ANNUAL REVIEWS

Annual Review of Virology

Virus Structures and Dynamics by Magic-Angle Spinning NMR

Gal Porat-Dahlerbruch,[1] Amir Goldbourt,[2] and Tatyana Polenova[1,3]

[1]Department of Chemistry and Biochemistry, University of Delaware, Newark, Delaware 19716, USA; email: tpolenov@udel.edu

[2]School of Chemistry, Tel Aviv University, Tel Aviv 6997801, Israel

[3]Pittsburgh Center for HIV Protein Interactions, University of Pittsburgh School of Medicine, Pittsburgh, Pennsylvania 15261, USA

Annu. Rev. Virol. 2021. 8:219–37

The *Annual Review of Virology* is online at virology.annualreviews.org

https://doi.org/10.1146/annurev-virology-011921-064653

Keywords

MAS NMR, solid-state NMR, virus assemblies, structure, capsids, dynamics

Abstract

Techniques for atomic-resolution structural biology have evolved during the past several decades. Breakthroughs in instrumentation, sample preparation, and data analysis that occurred in the past decade have enabled characterization of viruses with an unprecedented level of detail. Here we review the recent advances in magic-angle spinning (MAS) nuclear magnetic resonance (NMR) spectroscopy for structural analysis of viruses and viral assemblies. MAS NMR is a powerful method that yields information on 3D structures and dynamics in a broad range of experimental conditions. After a brief introduction, we discuss recent structural and functional studies of several viruses investigated with atomic resolution at various levels of structural organization, from individual domains of a membrane protein reconstituted into lipid bilayers to virus-like particles and intact viruses. We present examples of the unique information revealed by MAS NMR about drug binding, conduction mechanisms, interactions with cellular host factors, and DNA packaging in biologically relevant environments that are inaccessible by other methods.

1. INTRODUCTION

The contemporary structural biology toolbox developed over the past three to four decades enables a wide variety of systems to be studied with varying degrees of spatial and temporal resolution. The majority of atomic-resolution structures of biological molecules so far were determined by X-ray crystallography, while cryoelectron microscopy (cryo-EM) is considered a method of choice for large biological assemblies. Solution nuclear magnetic resonance (NMR) spectroscopy is commonly used for determination of 3D structures and dynamics of proteins and characterization of functional interactions with binding partners. While a powerful technique, solution NMR is limited by size and solubility, thus precluding characterization of large and/or insoluble systems, such as biological assemblies and intact viruses. Those kinds of systems can be studied by magic-angle spinning (MAS) solid-state NMR spectroscopy, as illustrated in **Figure 1**. In MAS NMR, a rotor containing the solid sample is spun in the magnetic field at frequencies on the order of thousands of revolutions per second (kHz). In contrast to solution state, where narrow spectral lines are attained because molecules naturally rotate, in the specimens where fast molecular rotations are absent (e.g., large assemblies or generally any immobilized systems), mechanical rotation of

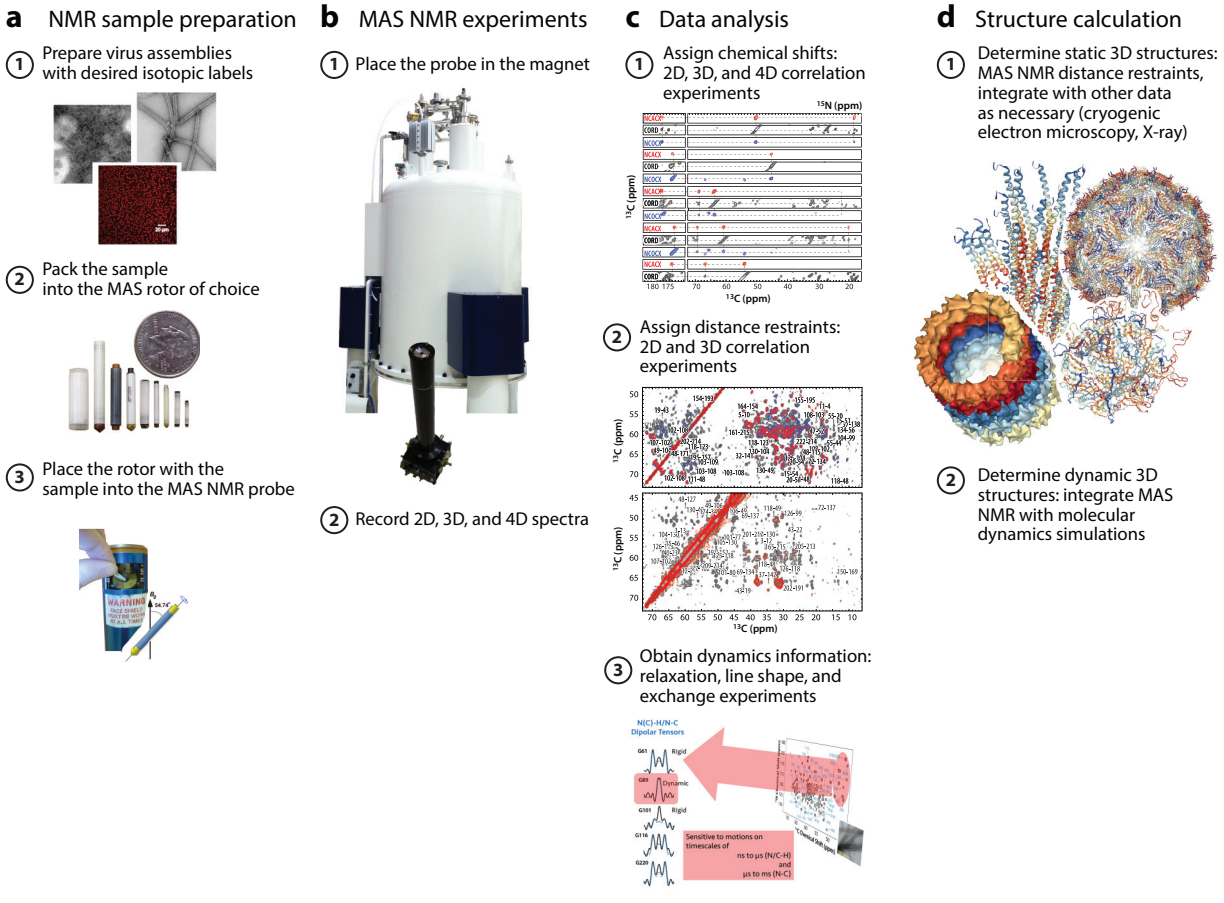

Figure 1

Schematic representation of the workflow for structure and dynamics investigations of viruses by MAS NMR. Abbreviations: MAS, magic-angle spinning; NMR, nuclear magnetic resonance.

Table 1 Atomic-resolution techniques in structural biology

	X-ray crystallography	Cryoelectron microscopy	Solution nuclear magnetic resonance	Magic-angle spinning nuclear magnetic resonance
Molecular weight requirement for atomic-resolution structural analysis	None	>40 kDa	<50 kDa	None
Specimen state	Single crystal	Vitrified	Solution, micelles	Crystalline, sedimented hydrated solutions, vitrified, powder
Accessibility of dynamics information	No/indirectly	No/indirectly	Yes	Yes
Temperature range	No limitations, determined by the sample stability	Cryogenic	Above freezing	No limitations, determined by the sample stability
Sample conditions (pH, salts, etc.)	Determined by crystallization conditions	No inherent limitations	No inherent limitations	No inherent limitations

the specimen in the NMR rotor during the course of an experiment is required for high spectral resolution, as discussed below. MAS NMR stands apart from other structural biology methods as it exhibits all of the following features: (*a*) there is no requirement that specimens be soluble or crystalline; (*b*) there are no inherent size or molecular weight limitations, so both small molecules and megadalton-large complexes are amenable to atomic-level characterization; (*c*) the experiments can be performed in a wide range of experimental conditions including pH, ionic strength, concentrations, and temperatures, which can range from physiological to cryogenic; (*d*) information on both structure and dynamics can be obtained, with atomic resolution, on the same specimen; and (*e*) details of local environment, such as interactions with small-molecule inhibitors, lipids, solvent, and protonation states of functional residues, are readily available from the experiments. The advantages and limitations of the various atomic-resolution structural biology methods are summarized in **Table 1**. Given the unique capabilities of MAS NMR enumerated above, the technique is rapidly gaining popularity for structural studies of a wide range of viruses and viral protein assemblies, as summarized in **Table 2**.

To introduce the reader to MAS NMR spectroscopy, we first present a brief overview of the following concepts and practical considerations: (*a*) the requirement for fast mechanical rotation

Table 2 Examples of viruses structurally characterized by magic-angle spinning nuclear magnetic resonance spectroscopy, grouped according to the Baltimore classification (112)

Class I	Class II	Class IV	Class V	Class VI	Class VII
T4[a]	Pf1[a]	Severe acute respiratory syndrome coronavirus 2[c]	Measles virus[b]	Human immunodeficiency virus type 1[b,c]	Hepatitis B virus[b]
T7[a]	fd[a]	Hepatitis C virus[b]	Influenza A[c] and B[c]	Rous Sarcoma virus[b]	
SPP1[b]	M13[a]	AP205[b]	Parainfluenza 5[c]		

[a]Studied as an intact phage.
[b]Studied as a viral protein assembly.
[c]Studied as a viral protein embedded in lipid membranes.

of the sample during the experiment, (*b*) the factors determining sensitivity of the measurements, (*c*) sample conditions, and (*d*) information content of MAS NMR spectra. The essential steps in MAS NMR–based structure characterization of viruses are illustrated in **Figure 1**. For the purposes of this review, we focus on the most frequently studied biologically relevant nuclei, such as ^{1}H, ^{13}C, ^{15}N, and ^{31}P, whose nuclear spin is 1/2.

1.1. Mechanical Rotation of the Sample Around a Judiciously Chosen Axis, the Magic Angle, Is Required for High-Resolution NMR Spectroscopy of Large Biological Assemblies

The NMR frequencies measured in a typical experiment are determined by nuclear spin interactions, whose magnitudes are dependent on the orientation of the molecules comprising a sample, relative to the static magnetic field (**Figure 1**). In solution, the molecules rotate rapidly and isotropically (i.e., there is no preferred axis of rotation), and each atom in the specimen experiences an average field. Hence, a single NMR frequency is detected, corresponding to the average field experienced by the atom and resulting in high spectral resolution (one narrow peak per atom). When molecules in a specimen do not rotate isotropically, such as in solid powders, crystals, large assemblies, frozen solutions, and molecules immobilized on solid supports, the NMR signals are broad (1).

If a sample is mechanically rotated around a single axis forming an angle of 54.74° with respect to the static magnetic field (dubbed the magic angle), the orientational dependencies of the nuclear spin interactions are averaged out over a rotor period (2–4). If a sample is rotated rapidly enough, so that the spinning frequency exceeds the magnitude of the interaction, a complete averaging occurs, and every atom in a specimen experiences an average field, resulting in a narrow signal, similar to solution NMR. But in contrast to solution NMR, the widths of the individual peaks are independent of the molecular weight in the MAS NMR experiments. This is the basis for high-resolution MAS NMR spectroscopy of large assemblies and any specimens comprising immobilized molecules.

MAS frequencies of at least 8–10 kHz are necessary for recording well-resolved spectra for ^{13}C, ^{15}N, and ^{31}P nuclei. While this range of frequencies is sufficient for basic biological MAS NMR experiments, in practice the faster the specimen is spun, the higher the resolution and the sensitivity for the same rotor diameter. Attaining faster MAS frequencies requires NMR rotors of progressively smaller diameters and hence reduced sample amounts, as shown in **Figure 1**. The choice of the MAS frequency depends on the sample and experiment of interest, and the highest practically achievable MAS frequency in a commercial MAS NMR probe is currently 111 kHz.

1.2. Multiple Factors Determine the Sensitivity of MAS NMR Experiments in Biological Assemblies

Intrinsic sensitivity of an NMR experiment, S, can be expressed as

$$S \propto \frac{\gamma^3 B_0^2}{T},$$

where γ is the gyromagnetic ratio of the detected nucleus (a fundamental physical constant, a ratio of the magnetic moment of a nucleus to its angular momentum), B_0 is the magnitude of the static magnetic field, and T is the temperature. Therefore, the higher the magnetic field and the nucleus's gyromagnetic ratio, and the lower the temperature, the higher the sensitivity. Of all stable isotopes, ^{1}H possesses the highest gyromagnetic ratio and is nearly 100% naturally abundant; hence, it yields the highest sensitivity in NMR experiments. The sensitivity also depends on the hardware design (i.e., the spectrometer and the MAS NMR probe design) (5).

In practice, MAS NMR experiments on large biological systems are usually performed at magnetic fields of 14.1 T to 23.5 T (^{1}H Larmor frequency of 600 MHz and 1 GHz, respectively). Very recently, 28.2 T superconducting magnets (^{1}H Larmor frequency of 1.2 GHz) have become commercially available (6). The choice of the MAS frequency and the experimental setup is determined by the type of sample under investigation—that is, the amount and the isotopic labeling accessible for a given sample (see Section 1.3), the molecular size, and the number of nuclear spins that give rise to the NMR signal (in the case of isotopically diluted samples). Additionally, more considerations come into play when selecting a rotor, such as improved radiofrequency coil homogeneity of smaller rotors, available temperature range, and other sample-dependent considerations.

1.3. Sample Considerations for MAS NMR Experiments

Because the NMR active isotopes of carbon and nitrogen, ^{13}C and ^{15}N, are only 1.11% and 0.37% naturally abundant, respectively, isotopic enrichment of one or both in the sample under investigation is required for in-depth structural and dynamic characterization of any biological samples. These isotopes can be introduced into viruses (7–11) or recombinantly generated viral proteins and/or nucleic acids (12–31) by adding them to the growth medium or synthetically (32, 33). Labels can be introduced either uniformly (i.e., every carbon and/or nitrogen atom will be enriched in the respective isotope) or into judiciously chosen sites (e.g., into selected amino acid types or following various sparse labeling schemes). Heterogeneous or mixed labels can also be incorporated, where each component in a complex may have a different labeling pattern or, alternatively, a single-component sample may contain differently labeled subpopulations. For example, by labeling the same protein with either ^{13}C or ^{15}N and mixing the two samples, one can obtain a sample in which the adjacent molecules contain different NMR active isotopes, which allows for investigation of intermolecular interactions and dynamics. As another approach, embedding a membrane protein containing one type of a label in lipid bilayers containing a different label can report on protein/membrane interactions. Deuterium (^{2}H) labeling is also frequently used in MAS NMR studies of biological assemblies to dilute the otherwise densely coupled proton networks, giving rise to large resolution enhancements. Alternatively, ^{2}H itself is used to probe dynamics in proteins and oligonucleotides. (For a review of the isotopic labeling schemes commonly used in MAS NMR of biological assemblies, we refer the interested reader to Reference 34.) Recently, ^{19}F labeling has become popular for studies of virus assemblies (18, 35). Due to its favorable properties (very high gyromagnetic ratio, 100% natural abundance, and absence in biological systems), fluorine is an exquisitely sensitive NMR probe. Furthermore, interfluorine distances of up to 2 nm are detectable; these report on the quaternary structure of proteins in assemblies of multiple monomers (18, 35).

The sample quantities required for MAS NMR spectroscopy depend on the extent of isotopic labeling—that is, whether the specimen is uniformly isotopically labeled or combines isotopically labeled and naturally abundant molecules or sites. Once the sample containing appropriate isotopic labels is prepared, it is centrifuged into a MAS NMR rotor, which is tightly sealed for the experiments. The specimens in the rotor are fully hydrated, their morphology is retained through the course of experiments, and they typically last through the entire duration of the measurements, which could be weeks or months (36).

1.4. Information Content of MAS NMR Experiments

The atomic-resolution 3D structure determination by MAS NMR relies mainly on two types of restraints: (*a*) backbone torsion angles calculated from chemical shifts (NMR frequencies) and (*b*) the availability of many hundreds of pairwise distance restraints between atoms in a biological

assembly (37). These restraints are acquired in various types of correlation experiments, as shown in **Figure 1** and reviewed in References 34 and 38. While solution NMR experiments mostly correlate atoms connected by a covalent chemical bond, MAS NMR relies on through-space, dipolar interactions. These through-space correlations report uniquely on atom pairs that are close in space but may not necessarily be linked through a covalent bond. Importantly, hydrogen atoms (^{1}H or ^{2}H) can be directly detected in MAS NMR experiments, providing exquisite chemical and structural details (such as hydrogen bonding, protonation, and tautomeric states) typically not accessible from X-ray or cryo-EM structures. The upper distance range practically detected in MAS NMR experiments involving ^{1}H, ^{13}C, and ^{15}N nuclei is about 8 Å. Distances of up to 20 Å can be measured in ^{19}F–^{19}F correlation experiments.

Besides 3D structures, MAS NMR can provide a wealth of structural information for viruses, over a broad range of length scales, from DNA packaging in viruses to interactions with small molecules, all with atomic resolution. Furthermore, dynamic regions of the viruses can be uniquely investigated by MAS NMR integrated with molecular dynamics (MD) simulations. This information is available through various NMR parameters reporting on local dynamics spanning many decades of motional timescales. Furthermore, different conformers and conformational distributions can be detected directly in frozen samples (39, 40).

2. EXAMPLES OF VIRAL SYSTEMS STUDIED BY MAS NMR

In this section, we discuss viral systems investigated by MAS NMR: membrane protein oligomers of influenza and severe acute respiratory syndrome coronavirus 2 (SARS-CoV-2) viruses, human immunodeficiency virus type 1 (HIV-1) capsid protein (CA) assemblies, a *Bacillus* phage SPP1 flexible tail-tube assembly, *Acinetobacter* phage AP205 virus-like particles (VLPs), and intact filamentous bacteriophages Pf1, fd, and M13. We highlight the role of MAS NMR in yielding information about 3D structure, functionally important dynamics, and mechanisms, as well as interactions with cofactors and single-stranded DNA (ssDNA) packaging, inaccessible by other means.

2.1. Influenza A and B

The *Orthomyxoviridae* family viruses influenza A and B cause seasonal flu. In the United States alone, the Centers for Disease Control and Prevention (CDC) estimates a death toll rate between 12,000 and 79,000 individuals during every influenza season since 2010 (41). Because a universal flu vaccine targeting all strains is not yet available, research focuses heavily on antiviral medication development. In the last quarter of the twentieth century, two antiviral compounds were used to treat influenza A infections, amantadine (AMT) and rimantadine (RMT). Unfortunately, most circulating influenza A strains have evolved AMT and RMT resistance, rendering them ineffective.

AMT and RMT inhibit influenza A replication by blocking the M2 transmembrane channel (AM2), but M2 proteins of low sequence homology and similar structure and function exist in influenza B strains as well (BM2). M2 exclusively transfers protons into the virion under acidic conditions. The function of the channel is essential for both cell entry and maturation of the virus in the infected cell Golgi membrane. Blocking M2 severely halts virus replication. M2 oligomerizes into a four-helix bundle, with each subunit passing through the membrane once. Its transmembrane (TM) domain makes up the proton-selective channel, dependent on the HxxxW motif (residues His-37 and Trp-41) that was found to be essential for proton selectivity (42, 43). M2 studies by MAS NMR allowed researchers to exploit membrane-mimetic environments to gain insights into the conduction mechanism and organization of the channel.

The conduction mechanism of AM2 was investigated by MAS NMR using His-37 as a probe of dynamics, protonation state, tautomerization (the process of low-barrier conversion from one

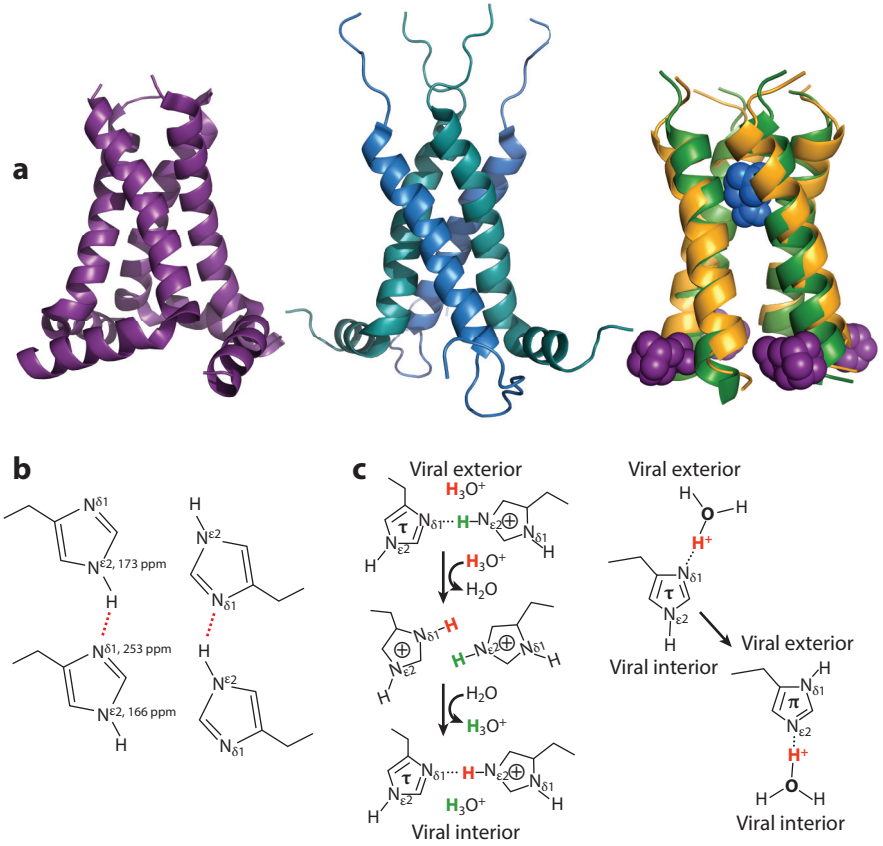

Figure 2

(*a*) AM2 structures solved by MAS NMR: homotetramer (PDB: 2L0J) (*left*), dimer of dimers (PDB: 2N70) (*middle*), and superposition of amantadine-bound AM2 (PDB: 2KQT) and rimantadine-bound AM2 (PDB: 2RLF) structures determined by MAS NMR (*yellow* and *blue*) and solution NMR (*green* and *purple*) (*right*). (*b*) The dimeric arrangement of His-37 in the AM2 pore occurring due to hydrogen bonding, corresponding to the dimer-of-dimers organization of the M2 helices. Panel *b* adapted with permission from Reference 23; copyright 2020 American Chemical Society. (*c*) Two proton conduction models for AM2 His-37 involving different histidine tautomers, protonation states, and hydrogen bonds. One model entails hydrogen bond formation between two histidine residues (*left*); the other suggests proton shuttling by histidine tautomerization and hydrogen bonding with hydronium ions (*right*). Panel *c* adapted with permission from Reference 24; copyright 2020 American Chemical Society. Abbreviations: AM2, influenza A M2; MAS, magic-angle spinning; NMR, nuclear magnetic resonance.

structural isomer to another), and hydrogen bonding (22–24, 44–47). Two possible conduction models involve different histidine tautomers and charges and different hydrogen bonding partners (**Figure 2*c***). The low-barrier hydrogen bond model suggests that two histidines in the pore form a hydrogen bond. According to this model, at low pH a hydronium ion protonates one of these residues, thus breaking the hydrogen bond. One of the protonated histidines then loses its proton to the less acidic viral interior, completing the proton transfer and reforming the inter-histidine hydrogen bond. Another model suggests a proton shuttling mechanism. Histidine's sidechain is protonated in the acidic environment, flips, and protonates a water molecule in the viral interior. This model does not involve any interaction between adjacent histidine sidechains in the pore.

The two models can be differentiated by MAS NMR through histidine chemical shifts, as well as by probing whether a hydrogen bond exists between two adjacent histidine sidechains.

The imidazole-imidazolium and imidazole-imidazole hydrogen bonds of AM2 His-37 were probed at low and high pH, respectively (23, 24). At low pH, the existence of a hydrogen bond was detected, suggesting a low-barrier hydrogen bond mechanism is operational (24). At high pH, increased dynamics of the histidine residues in the pore and breaking of the hydrogen bond were observed. Both also play a role in the RMT inhibitory mechanism, as discussed below (23).

Several groups also investigated the mechanism of AM2 inhibition by AMT and RMT using MAS NMR (20, 48–54). Two binding sites were identified, one inside the channel pore from the N-terminal side and the other at the cytoplasmic side of the pore (**Figure 2*a***). Based on the data, an allosteric mechanism of inhibition was proposed (52, 53). Binding to the latter site was observed only at high inhibitor concentrations (20) or at cryogenic temperatures, by dynamic nuclear polarization (DNP) (54). Binding to the site within the channel pore was found to be more important for inhibition.

Interestingly, MAS NMR studies of AM2 and the drug-resistant mutant S31N AM2 in DPhPC (1,2-diphytanoyl-*sn*-glycero-3-phosphocholine) bilayers revealed a dimer-of-dimers organization (19, 55), contrary to the homotetrameric arrangements found by solution NMR and X-ray diffraction (56, 57). The homotetrameric structure of AM2 was also observed in DMPC (1,2-dimyristoyl-*sn*-glycero-3-phosphocholine) and other virus-mimetic lipid bilayers. The organization of the channel may be linked to the conduction mechanism (see above and **Figure 2**). Recent studies showed the full-length AM2 fold is affected by membrane composition, including cholesterol content, and drug binding (49, 58), possibly explaining that the channel can form different oligomeric structures depending on the lipid mixture used for the reconstitution (59).

MAS NMR studies of BM2 revealed a different proton conduction mechanism from the one found for AM2 (12). While AM2 was found to almost exclusively transfer protons inside the virion, BM2 allows bidirectional proton transfer (with stronger proton flow inside the virion than outside). Interhelical distance restraints from a mixture of fluorinated phenylalanine and ^{13}C-labeled proteins aided in the determination of the BM2's quaternary structure, in both open and closed states, at different pH. Interestingly, differences in pore volume were found between the two states. Furthermore, in contrast to the single histidine residue in AM2 TM helix, BM2 has an additional histidine (His-27) following the HxxxW motif (His-19 and Trp-23), forming an HxxxWxxxH motif. MAS NMR revealed that the H27A mutant BM2 loses bidirectionality of proton transfer, resembling the AM2 conduction mechanism (60). Whether the functionally important histidine residues of BM2 form dimers through hydrogen bonds as observed in AM2 His-37 remains an open question.

2.2. Severe Acute Respiratory Syndrome Coronavirus 2

Viruses of the *Coronaviridae* family encode 4–5 structural proteins, with the corresponding single-stranded RNA (ssRNA) making up about one-third of the viral genome. The envelope (E) protein, the smallest *Coronaviridae* structural protein, is a homopentamer viroporin. Its functional roles and the ability of other nonstructural proteins to compensate for its deletion from recombinant virions are under investigation (61). The deletion of E protein attenuates the growth of SARS-CoV (62). Therefore, the pentameric E protein channel is a possible drug target.

SARS-CoV-2, the virus responsible for the coronavirus disease 2019 (COVID-19) pandemic, has been under intense investigation by various structural biology methods, including MAS NMR. Most recently, the E protein's transmembrane (TM) helix structure was solved in lipid bilayers (18).

The 3D structure revealed the backbone conformation, water accessibility, and drug binding. To corroborate that the E protein is a homopentamer, differentially labeled samples were prepared, where ^{13}C-labeled E protein monomers were mixed with fluorinated-phenylalanine-labeled or ^{15}N-labeled monomers. These preparations allowed for the acquisition of MAS NMR correlation spectra, from which 87 ^{13}C–^{19}F and ^{13}C–^{15}N interhelical distance restraints were identified and used for the calculation of the 3D structure of the pentamer.

Three phenylalanine residues in the middle of each chain appear to stack in the same helix and between helices, causing the formation of a nonideal alpha-helical structure. This is in contrast to the structure reconstructed from solution-state NMR data for the SARS-CoV E protein in micelles (63). MAS NMR water accessibility experiments revealed a dehydrated pore, which agrees with the tight packing of the helices as indicated by the distance restraints-based structure (18). The structure most likely resembles the channel's closed state due to observed minimal pore diameter of 2 Å.

The same study also characterized drug binding to the E protein. Chemical shift perturbation analysis revealed that hexamethylene amiloride and AMT, which inhibit the E protein of SARS-CoV (64, 65), bind to the N terminus of the SARS-CoV-2 E protein's TM helix, providing clues for future inhibitor design.

2.3. Human Immunodeficiency Virus Type 1

The *Retroviridae* HIV-1 is the causative agent of acquired immunodeficiency syndrome and the associated global pandemic that has claimed more than 35 million lives so far. HIV-1 protein assemblies have been studied by several MAS NMR research groups focusing on the Gag polyprotein and mature CA assemblies (14, 27, 35, 40, 66–80), viral protein U (17, 81–83), and glycoprotein 41 (gp41) (26, 84–86).

Mature HIV-1 conical capsid, which contains the viral genome, is assembled from 1,000–1,500 individual CAs and plays multiple important roles in HIV-1 replication. Most of the MAS NMR studies to date focused on in vitro CA assemblies of tubular morphologies, whose hexagonal lattice recapitulates the predominant symmetry of the mature cone-shaped capsid. MAS NMR investigations provided information about structural details and dynamics of tubular CA assemblies (27, 40, 66, 68–71, 73, 75–77, 79, 80) inaccessible by other techniques. Integrated MAS NMR and MD investigations revealed that CA is remarkably dynamic, with motions occurring over many timescales and being important for the HIV-1 maturation and capsid assembly (27, 70, 75). Recently, the atomic-resolution structure of CA tubular assemblies was determined by MAS NMR, in combination with low-resolution cryo-EM and data-guided MD simulations (14) (**Figure 3**). Notable differences from the crystallographic structure of flat hexamers were found, and novel and unique atomic resolution information on flexible and functionally important regions of the capsid was obtained. Such regions comprise the cyclophilin A (CypA) binding loop, the interdomain linker, and residues lining the hexamer pore (**Figure 3*c–e***). These structural data can be exploited in complementary capsid-targeted therapeutic strategies.

Several studies shed light on the interactions of CA assemblies with cellular host factors CypA (70, 75) and TRIM5α (66). CypA regulates viral infectivity by interacting directly with the capsid and can either promote or inhibit viral infection, depending on host cell type and CA sequence. A MAS NMR investigation uncovered that capsid's escape from CypA dependence is regulated allosterically through the modulation of the dynamics of the CypA-binding loop (75). Remarkably, the loop motions are greatly attenuated in the CypA escape mutants, A92E and G94D, compared to the wild type. Similarly, dynamic allosteric regulation was found to be critical for the interactions of capsid with TRIM5α (66). This restriction factor recognizes the capsid's lattice and triggers an

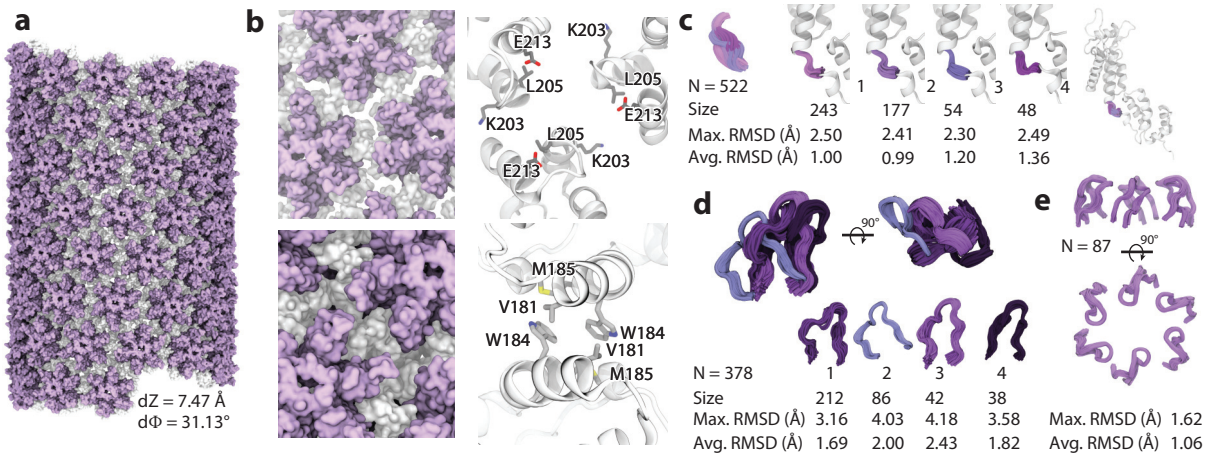

Figure 3

Structure of a human immunodeficiency virus type 1 capsid protein tube generated by data-guided molecular dynamics. (*a*) Molecular surface of a (−12,11) helical symmetry tube (helical parameters dZ = 7.47 Å and dϕ = 31.13°). The N- and C-terminal domains are colored purple and gray, respectively. (*b*) Representative trimer (*top*) and dimer (*bottom*) interfaces, in surface (*left*) and ribbon (*right*) representation. K203, L205, and E213 sidechains (trimer interface) and V181, W184, and M185 sidechains (dimer interface) are shown in ball-and-stick representations. (*c*) Four representative conformations of the flexible linker region, colored and grouped by structural cluster. (*d*) Four representative conformations of the cyclophilin A binding loop, colored and grouped by structural cluster. The size of each cluster and the RMSD within each cluster (Å) are listed. (*e*) Arrangement of the β-hairpins in the hexamers. Figure adapted with permission from Reference 14; copyright 2020 Springer Nature.

innate immune response causing capsid's premature uncoating (87, 88). Binding of TRIM5α to capsid was found to induce global rigidification and perturb key intermolecular interfaces involved in higher-order capsid assembly. Remarkably, structural and dynamic changes occur throughout the entire CA in the assembly (66).

While CA assemblies recapitulating mature capsid have been the focus of multiple MAS NMR studies, Gag maturation intermediates and VLPs have also been investigated (27, 76, 79). Given the size of Gag polyprotein, its NMR characterization is challenging with uniform ^{13}C,^{15}N labeling. Segmental labeling was therefore explored to simplify the chemical shift assignments (67, 79). Therein, two segments of a single protein with different labels are individually expressed. The two segments are then purified and reattached using intein technology to form the full-length protein (89). Structural investigation of the CA–spacer peptide 1 (SP1) junction helices bound to the maturation inhibitor bevirimat in HIV-1 VLPs showed a slight structural alteration that is apparently sufficient to inhibit the CA-SP1 cleavage (79).

2.4. *Bacillus* Phage SPP1 Flexible Tail Tube

Siphoviridae is a family of double-stranded DNA viruses with an icosahedral nucleocapsid and a long flexible tail. The *Siphoviridae* SPP1 phage tail consists of protein gp17.1 and its translational frameshift, gp17.1*, in a ratio of 3:1. Nonetheless, gp17.1 can polymerize in solution and forms the tail tube even in the absence of gp17.1*. This modification was shown not to affect phage assembly and infectivity, thus well representing the tail-tube assembly structure and function in vivo. While structures of phage tails were previously reconstructed by cryo-EM with a resolution of 3–4 Å, the flexibility of the *Siphoviridae* tail still poses a challenge, limiting the structural information available from cryo-EM.

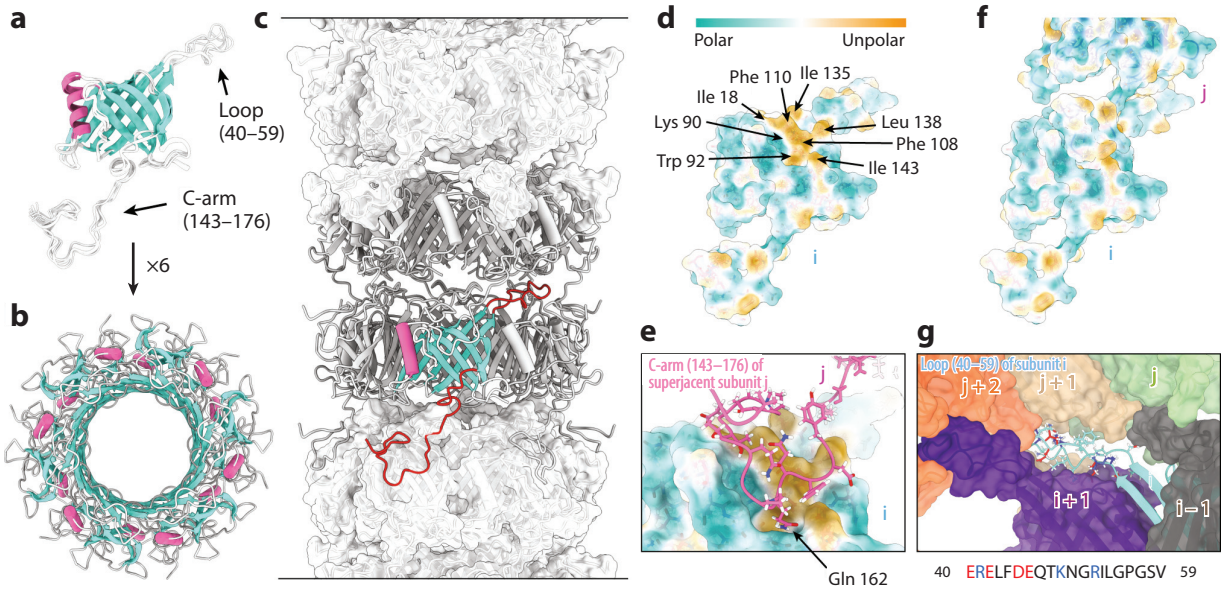

Figure 4

(*a*) Final 10 lowest-energy structures of a gp17.1 subunit, which consist of a central β-sandwich-type fold (*turquoise*) that is flanked by an α-helix (*pink*), a large loop, and an extended C-arm. (*b*) Six gp17.1 monomers forming a hexameric ring. The inner β-sheets of the β-sandwiches organize in a β-barrel motif that forms the lumen of the tube. (*c*) Hexameric rings stacking onto each other in a helical fashion to create a hollow tube. Ring-to-ring contacts are mediated by the two loop regions (highlighted in *red*)—especially by the C-arm that folds onto the subjacent ring. (*d*) The molecular lipophilicity potential of gp17.1 revealing a hydrophobic patch on the surface of one subunit i. The color gradient represents the lipophilicity potential. (*e*,*f*) Unpolar area obscured by the C-arm (*pink*) of the superjacent subunit j within the complex of the tail tube by anchoring the sidechain of Gln-162 into a pocket. (*g*) The loop of subunit i (*turquoise*) featuring mostly electrostatic interactions with five neighboring subunits (*gray*, *purple*, *green*, *beige*, and *orange*) within the complex. Charged amino acids are negative (*red*) and positive (*blue*). The direction of the tail structure is baseplate upward. Abbreviation: C-arm, C-terminal arm. Figure adapted with permission from Reference 13; copyright 2020 Springer Nature.

To determine the atomic-resolution structure of the *Siphoviridae* SPP1 phage flexible tail-tube assembly, Lange and colleagues (13, 90, 91) expressed, purified, and polymerized recombinant gp17.1 for MAS NMR investigations. The final calculated structure, consisting of 12 subunits, was refined using both NMR-derived distance restraints and a cryo-EM density map. The 12 subunits represent two rings of the tail-tube assembly (**Figure 4*a–c***). The structure revealed that the C-arm domain interacts with the suprajacent subunit to obscure hydrophobic chains of that subunit, and the loop region of one subunit participates in electrostatic interactions with five other subunits (**Figure 4*d–g***).

2.5. *Acinetobacter* Phage AP205 Virus-Like Particles

VLPs of ssRNA bacteriophages, such as AP205, are targets for antigen display vaccine development against cancer, viral infections, and more (92–97). Such VLPs are promising platforms for vaccine development, mostly due to their safety, relatively small size, and repetitive structure (98). AP205 has low sequence similarity with other ssRNA phages, and structural knowledge has been lacking. To solve the structure of the entire AP205 VLP, MAS NMR and cryo-EM were combined (16). The available state-of-the-art MAS NMR hardware enabled the studies to be performed with sub-milligram quantities of AP205 VLP crystals, instead of the routinely required tens of milligrams. Combining the 1.7-Å NMR-derived model of unassembled

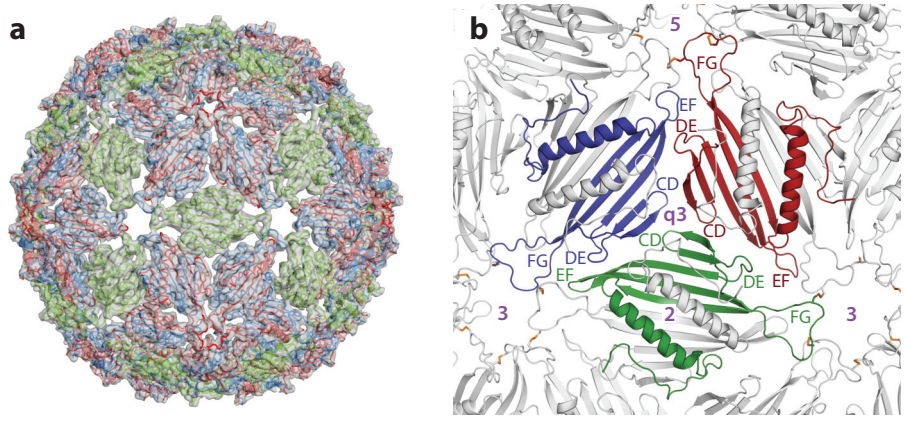

Figure 5

(*a*) The complete AP205 capsid model as derived from the low-resolution cryoelectron microscopy electron density map and magic-angle spinning nuclear magnetic resonance–derived coat protein dimer model. (*b*) A close-up look of the dimer packing in the assembled AP205 capsid. The protein loops and the location of the 2- (2), 3- (3), 5- (5), and quasi 3- (q3) fold symmetry axes of the particle are indicated. In both panels, the A, B, and C monomers of the icosahedral asymmetric unit are colored blue, red, and green, respectively. Figure adapted with permission from Reference 16; copyright 2016 Elsevier.

dimers with the cryo-EM low-resolution reconstruction yielded a high-resolution structure of the full AP205 capsid (**Figure 5**). Interestingly, comparison of the ssRNA phages MS2 and AP205 coat protein revealed a similar fold despite a change in the order of amino acids in the sequence.

2.6. Intact Filamentous Bacteriophages

Filamentous bacteriophages are composed of a coat protein, which usually constitutes a major fraction of the virus. The number of copies of the coat protein is three orders of magnitude larger than that of other structural and nonstructural proteins in the virion. Such a large excess of the coat protein allows for MAS NMR studies of intact filamentous phages instead of the recombinantly expressed coat protein because other proteins are virtually invisible in the NMR spectra due to their low amounts. Several intact filamentous bacteriophages have been investigated by MAS NMR to date: Pf1 (7, 99–104), fd (9, 105–107), M13 (11, 105, 107), and fIKe (108).

The Pf1 coat protein was among the first to be studied by MAS NMR and the first protein for which chemical shift assignments were reported in an intact virion (7) (**Figure 6*a***). The results unequivocally indicated that all coat protein monomers adopt the same structure, in conflict with the previous X-ray fiber diffraction-based model, where three distinct coat protein folds appeared to coexist in the high-temperature structure of the virion (111). MAS NMR provided insights regarding the hydration of the different residues of the coat protein (100).

An additional DNP-based study conducted at a temperature of 100 K characterized ssDNA packaging in the Pf1 virion (101). The observed chemical shift values indicate that the ssDNA in the virion is devoid of hydrogen bonds and is relatively well structured. Through-space correlation spectra showed that Tyr-40 is in close contact with the ssDNA inside the phage, possibly due to stacking of the bases with its aromatic sidechain. This study provided strong experimental evidence to corroborate the previous Pf1 ssDNA packaging model (109, 110), suggesting a stretched ssDNA strand with its bases facing outward.

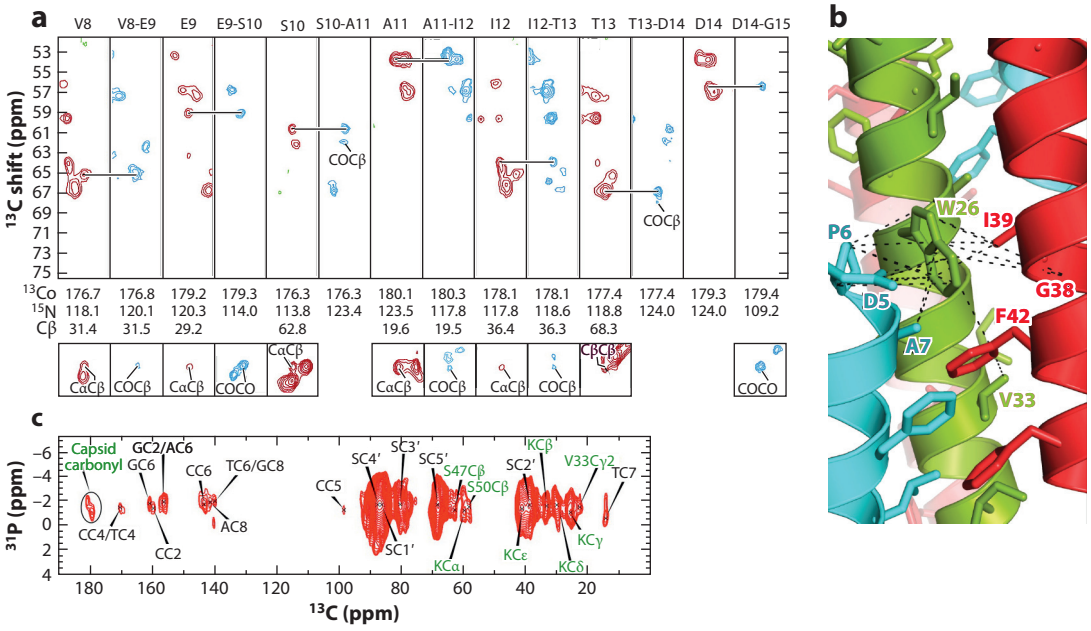

Figure 6

(*a*) Strip plot of the chemical shift assignment of the Pf1 coat protein in intact bacteriophages. NCOCX (*blue*) and NCACX (*red*) correlation spectra were used for sequential and intra-residue assignment, respectively. Panel *a* adapted with permission from Reference 7; copyright 2007 American Chemical Society. (*b*) Tryptophan binding pocket of the M13 nuclear magnetic resonance–Rosetta model. Dashed lines represent distance restraints between tryptophan and other residues in the same chain (*green*) and adjacent chains (*cyan* and *red*) in the capsid. Panel *b* adapted with permission from Reference 11; copyright 2015 National Academy of Sciences. (*c*) ^{31}P–^{13}C through-space correlation spectrum of ^{13}C- and ^{15}N-labeled and aromatic-unlabeled intact fd phage. Green and black labels indicate coat protein and DNA base correlations, respectively. Panel *c* adapted with permission from Reference 106; copyright 2014 American Chemical Society.

The coat proteins of fd and M13 phages were also studied, and chemical shifts were reported based on a combination of 2D and 3D experiments (9, 107). The coat proteins of the two phages differ by only a single mutation, and chemical shift perturbation and rigidity analysis revealed interesting atomic-level structural differences around the mutation sites. For example, the single D12N mutation of the fd coat protein caused perturbations to residue Lys-8 due to the removal of the negatively charged Asn-12 residue.

An M13 NMR-Rosetta model was built using interchain restraints obtained from the ^{13}C–^{13}C correlation spectra (11). This model revealed that each subunit hydrophobically interacts with four adjacent monomers in the capsid, and these interactions mostly depend on the conserved tryptophan residue and other tyrosine and phenylalanine residues in the coat protein (**Figure 6*b***).

Nucleotide-specific assignment of the fd phage, together with ^{31}P correlation experiments, enabled characterization of its ssDNA packaging (106) (**Figure 6*c***). An additional sample with unlabeled aromatic residues yielded the assignment of the ssDNA carbon nuclei that highly overlap with aromatic signals in the spectrum. Prior assignment of the coat protein assisted in identification of ssDNA base-, sugar-, and phosphate-capsid interactions. From the observed chemical shifts and correlations, and using information from the previous models, the salient ssDNA packaging characteristics were inferred. Notable differences with respect to the Pf1 model were observed, such as base pairing, and distinct ssDNA packaging. Of note, the virus remained infectious after

being taken out of the MAS NMR rotor, which confirmed the biological relevance of the structural observations.

3. CONCLUSIONS AND OUTLOOK

We have reviewed the basic principles and applications of MAS NMR spectroscopy to study the structure and dynamics of viruses. The remarkable progress in ultra-high-field superconducting magnet technology and the advent of high-frequency (60–150 kHz) MAS probes have opened doors for characterization of nanomole quantities of large viral assemblies and intact viruses. MAS NMR yields information inaccessible by other techniques, such as residue-specific drug-protein interactions, detailed DNA packaging characterization, specific hydrogen bonding, and functional dynamics, with atomic resolution. The recent notable advances also include integration of MAS NMR with other methods, such as MD simulations and/or cryo-EM. Further breakthroughs in experimental and data analysis protocols will enable application of MAS NMR to an even broader range of viruses.

DISCLOSURE STATEMENT

The authors are not aware of any affiliations, memberships, funding, or financial holdings that might be perceived as affecting the objectivity of this review.

ACKNOWLEDGMENTS

The authors acknowledge the support of the US-Israel Binational Science Foundation (grant 2011077). T.P. acknowledges the support of the National Institutes of Health (grant P50AI1504817).

LITERATURE CITED

1. Bloembergen N, Rowland TJ. 1953. On the nuclear magnetic resonance in metals and alloys. *Acta Metall.* 1:731–46
2. Andrew ER, Bradbury A, Eades RG. 1958. Nuclear magnetic resonance spectra from a crystal rotated at high speed. *Nature* 182:1659
3. Lowe IJ. 1959. Free induction decays of rotating solids. *Phys. Rev. Lett.* 2:285–87
4. Andrew ER, Bradbury A, Eades RG. 1959. Removal of dipolar broadening of nuclear magnetic resonance spectra of solids by specimen rotation. *Nature* 183:1802–3
5. Hoult DI, Richards RE. 1976. The signal-to-noise ratio of the nuclear magnetic resonance experiment. *J. Magn. Reson.* 24:71–85
6. Schwalbe H. 2017. Editorial: new 1.2 GHz NMR spectrometers—new horizons? *Angew. Chem. Int. Ed.* 56:10252–53
7. Goldbourt A, Gross BJ, Day LA, McDermott AE. 2007. Filamentous phage studied by magic-angle spinning NMR: resonance assignment and secondary structure of the coat protein in Pf1. *J. Am. Chem. Soc.* 129:2338–44
8. Yu T-Y, Schaefer J. 2008. REDOR NMR characterization of DNA packaging in bacteriophage T4. *J. Mol. Biol.* 382:1031–42
9. Abramov G, Morag O, Goldbourt A. 2011. Magic-angle spinning NMR of a class I filamentous bacteriophage virus. *J. Phys. Chem. B* 115:9671–80
10. Abramov G, Goldbourt A. 2014. Nucleotide-type chemical shift assignment of the encapsulated 40 kbp dsDNA in intact bacteriophage T7 by MAS solid-state NMR. *J. Biomol. NMR* 59:219–30
11. Morag O, Sgourakis NG, Baker D, Goldbourt A. 2015. The NMR–Rosetta capsid model of M13 bacteriophage reveals a quadrupled hydrophobic packing epitope. *PNAS* 112:971–76

12. Mandala VS, Loftis AR, Shcherbakov AA, Pentelute BL, Hong M. 2020. Atomic structures of closed and open influenza B M2 proton channel reveal the conduction mechanism. *Nat. Struct. Mol. Biol.* 27:160–67
13. Zinke M, Sachowsky KAA, Öster C, Zinn-Justin S, Ravelli R, et al. 2020. Architecture of the flexible tail tube of bacteriophage SPP1. *Nat. Commun.* 11:5759
14. Lu M, Russell RW, Bryer AJ, Quinn CM, Hou G, et al. 2020. Atomic-resolution structure of HIV-1 capsid tubes by magic-angle spinning NMR. *Nat. Struct. Mol. Biol.* 27:863–69
15. Jeon J, Qiao X, Hung I, Mitra AK, Desfosses A, et al. 2017. Structural model of the tubular assembly of the Rous Sarcoma virus capsid protein. *J. Am. Chem. Soc.* 139:2006–13
16. Shishovs M, Rumnieks J, Diebolder C, Jaudzems K, Andreas LB, et al. 2016. Structure of AP205 coat protein reveals circular permutation in ssRNA bacteriophages. *J. Mol. Biol.* 428:4267–79
17. Zhang H, Lin EC, Das BB, Tian Y, Opella SJ. 2015. Structural determination of virus protein U from HIV-1 by NMR in membrane environments. *Biochim. Biophys. Acta Biomembr.* 1848:3007–18
18. Mandala VS, McKay MJ, Shcherbakov AA, Dregni AJ, Kolocouris A, Hong M. 2020. Structure and drug binding of the SARS-CoV-2 envelope protein transmembrane domain in lipid bilayers. *Nat. Struct. Mol. Biol.* 27:1202–8
19. Andreas LB, Reese M, Eddy MT, Gelev V, Ni QZ, et al. 2015. Structure and mechanism of the influenza A $M2_{18–60}$ dimer of dimers. *J. Am. Chem. Soc.* 137:14877–86
20. Cady SD, Schmidt-Rohr K, Wang J, Soto CS, DeGrado WF, Hong M. 2010. Structure of the amantadine binding site of influenza M2 proton channels in lipid bilayers. *Nature* 463:689–92
21. Lee M, Yao H, Kwon B, Waring AJ, Ruchala P, et al. 2018. Conformation and trimer association of the transmembrane domain of the parainfluenza virus fusion protein in lipid bilayers from solid-state NMR: insights into the sequence determinants of trimer structure and fusion activity. *J. Mol. Biol.* 430:695–709
22. Hu F, Luo W, Hong M. 2010. Mechanisms of proton conduction and gating in influenza M2 proton channels from solid-state NMR. *Science* 330:505–8
23. Movellan KT, Wegstroth M, Overkamp K, Leonov A, Becker S, Andreas LB. 2020. Imidazole–imidazole hydrogen bonding in the pH-sensing histidine side chains of influenza A M2. *J. Am. Chem. Soc.* 142:2704–8
24. Fu R, Miao Y, Qin H, Cross TA. 2020. Observation of the imidazole-imidazolium hydrogen bonds responsible for selective proton conductance in the influenza A M2 channel. *J. Am. Chem. Soc.* 142:2115–19
25. Kovacs FA, Cross TA. 1997. Transmembrane four-helix bundle of influenza A M2 protein channel: structural implications from helix tilt and orientation. *Biophys. J.* 73:2511–17
26. Sackett K, Nethercott MJ, Zheng Z, Weliky DP. 2014. Solid-state NMR spectroscopy of the HIV gp41 membrane fusion protein supports intermolecular antiparallel β sheet fusion peptide structure in the final six-helix bundle state. *J. Mol. Biol.* 426:1077–94
27. Bayro MJ, Ganser-Pornillos BK, Zadrozny KK, Yeager M, Tycko R. 2016. Helical conformation in the CA-SP1 junction of the immature HIV-1 lattice determined from solid-state NMR of virus-like particles. *J. Am. Chem. Soc.* 138:12029–32
28. Marchanka A, Simon B, Althoff-Ospelt G, Carlomagno T. 2015. RNA structure determination by solid-state NMR spectroscopy. *Nat. Commun.* 6:7024
29. Marchanka A, Stanek J, Pintacuda G, Carlomagno T. 2018. Rapid access to RNA resonances by proton-detected solid-state NMR at >100 kHz MAS. *Chem. Commun.* 54:8972–75
30. Asami S, Rakwalska-Bange M, Carlomagno T, Reif B. 2013. Protein–RNA interfaces probed by ^{1}H-detected MAS solid-state NMR spectroscopy. *Angew. Chem. Int. Ed.* 52:2345–49
31. Lacabanne D, Boudet J, Malär AA, Wu P, Cadalbert R, et al. 2020. Protein side-chain–DNA contacts probed by fast magic-angle spinning NMR. *J. Phys. Chem. B* 124:11089–97
32. Wang S, Fogeron ML, Schledorn M, Dujardin M, Penzel S, et al. 2019. Combining cell-free protein synthesis and NMR into a tool to study capsid assembly modulation. *Front. Mol. Biosci.* 6:67
33. Fogeron M-L, Jirasko V, Penzel S, Paul D, Montserret R, et al. 2016. Cell-free expression, purification, and membrane reconstitution for NMR studies of the nonstructural protein 4B from hepatitis C virus. *J. Biomol. NMR* 65:87–98
34. Kraus J, Sarkar S, Quinn CM, Polenova T. 2021. Solid-state NMR spectroscopy of microcrystalline proteins. *Annu. Rep. NMR Spectrosc.* 102:81–151

35. Wang M, Lu M, Fritz MP, Quinn CM, Byeon I-JL, et al. 2018. Fast magic-angle spinning ^{19}F NMR spectroscopy of HIV-1 capsid protein assemblies. *Angew. Chem. Int. Ed.* 57:16375–79
36. Wiegand T, Lacabanne D, Torosyan A, Boudet J, Cadalbert R, et al. 2020. Sedimentation yields long-term stable protein samples as shown by solid-state NMR. *Front. Mol. Biosci.* 7:17
37. Russell RW, Fritz MP, Kraus J, Quinn CM, Polenova T, Gronenborn AM. 2019. Accuracy and precision of protein structures determined by magic angle spinning NMR spectroscopy: for some 'with a little help from a friend.' *J. Biomol. NMR* 73:333–46
38. Quinn CM, Polenova T. 2017. Structural biology of supramolecular assemblies by magic-angle spinning NMR spectroscopy. *Q. Rev. Biophys.* 50:e1
39. Havlin RH, Tycko R. 2005. Probing site-specific conformational distributions in protein folding with solid-state NMR. *PNAS* 102:3284–89
40. Gupta R, Zhang H, Lu M, Hou G, Caporini M, et al. 2019. Dynamic nuclear polarization magic-angle spinning nuclear magnetic resonance combined with molecular dynamics simulations permits detection of order and disorder in viral assemblies. *J. Phys. Chem. B* 123:5048–58
41. Natl. Cent. Immun. Respir. Dis. 2020. Past seasons estimated influenza disease burden. *Centers for Disease Control and Prevention.* **https://www.cdc.gov/flu/about/burden/past-seasons.html**
42. Wang C, Lamb RA, Pinto LH. 1995. Activation of the M2 ion channel of influenza virus: a role for the transmembrane domain histidine residue. *Biophys. J.* 69:1363–71
43. Tang Y, Zaitseva F, Lamb RA, Pinto LH. 2002. The gate of the influenza virus M2 proton channel is formed by a single tryptophan residue. *J. Biol. Chem.* 277:39880–86
44. Sharma M, Yi M, Dong H, Qin H, Peterson E, et al. 2010. Insight into the mechanism of the influenza A proton channel from a structure in a lipid bilayer. *Science* 330:509–12
45. Hong M, Fritzsching KJ, Williams JK. 2012. Hydrogen-bonding partner of the proton-conducting histidine in the influenza M2 proton channel revealed from ^{1}H chemical shifts. *J. Am. Chem. Soc.* 134:14753–55
46. Hu F, Schmidt-Rohr K, Hong M. 2012. NMR detection of pH-dependent histidine–water proton exchange reveals the conduction mechanism of a transmembrane proton channel. *J. Am. Chem. Soc.* 134:3703–13
47. Colvin MT, Andreas LB, Chou JJ, Griffin RG. 2014. Proton association constants of His 37 in the influenza-A $M2_{18–60}$ dimer-of-dimers. *Biochemistry* 53:5987–94
48. Tzitzoglaki C, Wright A, Freudenberger K, Hoffmann A, Tietjen I, et al. 2017. Binding and proton blockage by amantadine variants of the influenza $M2_{WT}$ and $M2_{S31N}$ explained. *J. Med. Chem.* 60:1716–33
49. Ekanayake EV, Fu R, Cross TA. 2016. Structural influences: cholesterol, drug, and proton binding to full-length influenza A M2 protein. *Biophys. J.* 110:1391–99
50. Williams JK, Tietze D, Wang J, Wu Y, DeGrado WF, Hong M. 2013. Drug-induced conformational and dynamical changes of the S31N mutant of the influenza M2 proton channel investigated by solid-state NMR. *J. Am. Chem. Soc.* 135:9885–97
51. Cady SD, Mishanina TV, Hong M. 2009. Structure of amantadine-bound M2 transmembrane peptide of influenza A in lipid bilayers from magic-angle-spinning solid-state NMR: the role of Ser_{31} in amantadine binding. *J. Mol. Biol.* 385:1127–41
52. Andreas LB, Eddy MT, Pielak RM, Chou J, Griffin RG. 2010. Magic angle spinning NMR investigation of influenza A $M2_{18–60}$: support for an allosteric mechanism of inhibition. *J. Am. Chem. Soc.* 132:10958–60
53. Cady SD, Hong M. 2008. Amantadine-induced conformational and dynamical changes of the influenza M2 transmembrane proton channel. *PNAS* 105:1483–88
54. Andreas LB, Barnes AB, Corzilius B, Chou JJ, Miller EA, et al. 2013. Dynamic nuclear polarization study of inhibitor binding to the $M2_{18–60}$ proton transporter from influenza A. *Biochemistry* 52:2774–82
55. Andreas LB, Eddy MT, Chou JJ, Griffin RG. 2012. Magic-angle-spinning NMR of the drug resistant S31N M2 proton transporter from influenza A. *J. Am. Chem. Soc.* 134:7215–18
56. Schnell JR, Chou JJ. 2008. Structure and mechanism of the M2 proton channel of influenza A virus. *Nature* 451:591–95

57. Stouffer AL, Acharya R, Salom D, Levine AS, Di Costanzo L, et al. 2008. Structural basis for the function and inhibition of an influenza virus proton channel. *Nature* 451:596–99
58. Liao SY, Fritzsching KJ, Hong M. 2013. Conformational analysis of the full-length M2 protein of the influenza A virus using solid-state NMR. *Protein Sci.* 22:1623–38
59. Mandala VS, Williams JK, Hong M. 2018. Structure and dynamics of membrane proteins from solid-state NMR. *Annu. Rev. Biophys.* 47:201–22
60. Kwon B, Roos M, Mandala VS, Shcherbakov AA, Hong M. 2019. Elucidating relayed proton transfer through a His–Trp–His triad of a transmembrane proton channel by solid-state NMR. *J. Mol. Biol.* 431:2554–66
61. Schoeman D, Fielding BC. 2019. Coronavirus envelope protein: current knowledge. *Virol. J.* 16:69
62. DeDiego ML, Álvarez E, Almazán F, Rejas MT, Lamirande E, et al. 2007. A severe acute respiratory syndrome coronavirus that lacks the E gene is attenuated in vitro and in vivo. *J. Virol.* 81:1701–13
63. Surya W, Li Y, Torres J. 2018. Structural model of the SARS coronavirus E channel in LMPG micelles. *Biochim. Biophys. Acta Biomembr.* 1860:1309–17
64. Torres J, Maheswari U, Parthasarathy K, Ng L, Liu DX, Gong X. 2007. Conductance and amantadine binding of a pore formed by a lysine-flanked transmembrane domain of SARS coronavirus envelope protein. *Protein Sci.* 16:2065–71
65. Li Y, Surya W, Claudine S, Torres J. 2014. Structure of a conserved Golgi complex-targeting signal in coronavirus envelope proteins. *J. Biol. Chem.* 289:12535–49
66. Quinn CM, Wang M, Fritz MP, Runge B, Ahn J, et al. 2018. Dynamic regulation of HIV-1 capsid interaction with the restriction factor TRIM5α identified by magic-angle spinning NMR and molecular dynamics simulations. *PNAS* 115:11519–24
67. Gupta S, Tycko R. 2018. Segmental isotopic labeling of HIV-1 capsid protein assemblies for solid state NMR. *J. Biomol. NMR* 70:103–14
68. Wang M, Quinn CM, Perilla JR, Zhang H, Shirra R Jr., et al. 2017. Quenching protein dynamics interferes with HIV capsid maturation. *Nat. Commun.* 8:1779
69. Bayro MJ, Tycko R. 2016. Structure of the dimerization interface in the mature HIV-1 capsid protein lattice from solid state NMR of tubular assemblies. *J. Am. Chem. Soc.* 138:8538–46
70. Liu C, Perilla JR, Ning J, Lu M, Hou G, et al. 2016. Cyclophilin A stabilizes the HIV-1 capsid through a novel non-canonical binding site. *Nat. Commun.* 7:10714
71. Lu J-X, Bayro MJ, Tycko R. 2016. Major variations in HIV-1 capsid assembly morphologies involve minor variations in molecular structures of structurally ordered protein segments. *J. Biol. Chem.* 291:13098–112
72. Gupta R, Lu M, Hou G, Caporini MA, Rosay M, et al. 2016. Dynamic nuclear polarization enhanced MAS NMR spectroscopy for structural analysis of HIV-1 protein assemblies. *J. Phys. Chem. B* 120:329–39
73. Zhang H, Hou G, Lu M, Ahn J, Byeon I-JL, et al. 2016. HIV-1 capsid function is regulated by dynamics: quantitative atomic-resolution insights by integrating magic-angle-spinning NMR, QM/MM, and MD. *J. Am. Chem. Soc.* 138:14066–75
74. Suiter CL, Quinn CM, Lu M, Hou G, Zhang H, Polenova T. 2015. MAS NMR of HIV-1 protein assemblies. *J. Magn. Reson.* 253:10–22
75. Lu M, Hou G, Zhang H, Suiter CL, Ahn J, et al. 2015. Dynamic allostery governs cyclophilin A–HIV capsid interplay. *PNAS* 112:14617–22
76. Han Y, Hou G, Suiter CL, Ahn J, Byeon I-JL, et al. 2013. Magic angle spinning NMR reveals sequence-dependent structural plasticity, dynamics, and the spacer peptide 1 conformation in HIV-1 capsid protein assemblies. *J. Am. Chem. Soc.* 135:17793–803
77. Byeon I-JL, Hou G, Han Y, Suiter CL, Ahn J, et al. 2012. Motions on the millisecond time scale and multiple conformations of HIV-1 capsid protein: implications for structural polymorphism of CA assemblies. *J. Am. Chem. Soc.* 134:6455–66
78. Han Y, Ahn J, Concel J, Byeon I-JL, Gronenborn AM, et al. 2010. Solid-state NMR studies of HIV-1 capsid protein assemblies. *J. Am. Chem. Soc.* 132:1976–87
79. Gupta S, Louis JM, Tycko R. 2020. Effects of an HIV-1 maturation inhibitor on the structure and dynamics of CA-SP1 junction helices in virus-like particles. *PNAS* 117:10286–93

80. Bayro MJ, Chen B, Yau W-M, Tycko R. 2014. Site-specific structural variations accompanying tubular assembly of the HIV-1 capsid protein. *J. Mol. Biol.* 426:1109–27
81. Do HQ, Wittlich M, Glück JM, Möckel L, Willbold D, et al. 2013. Full-length Vpu and human CD4(372–433) in phospholipid bilayers as seen by magic angle spinning NMR. *Biol. Chem.* 394:1453–63
82. Lu J-X, Sharpe S, Ghirlando R, Yau W-M, Tycko R. 2010. Oligomerization state and supramolecular structure of the HIV-1 Vpu protein transmembrane segment in phospholipid bilayers. *Protein Sci.* 19:1877–96
83. Sharpe S, Yau W-M, Tycko R. 2006. Structure and dynamics of the HIV-1 Vpu transmembrane domain revealed by solid-state NMR with magic-angle spinning. *Biochemistry* 45:918–33
84. Kwon B, Mandal T, Elkins MR, Oh Y, Cui Q, Hong M. 2020. Cholesterol interaction with the trimeric HIV fusion protein gp41 in lipid bilayers investigated by solid-state NMR spectroscopy and molecular dynamics simulations. *J. Mol. Biol.* 432:4705–21
85. Lee M, Morgan CA, Hong M. 2019. Fully hydrophobic HIV gp41 adopts a hemifusion-like conformation in phospholipid bilayers. *J. Biol. Chem.* 294:14732–44
86. Kwon B, Lee M, Waring AJ, Hong M. 2018. Oligomeric structure and three-dimensional fold of the HIV gp41 membrane-proximal external region and transmembrane domain in phospholipid bilayers. *J. Am. Chem. Soc.* 140:8246–59
87. Stremlau M, Owens CM, Perron MJ, Kiessling M, Autissier P, Sodroski J. 2004. The cytoplasmic body component TRIM5α restricts HIV-1 infection in old world monkeys. *Nature* 427:848–53
88. Stremlau M, Perron M, Lee M, Li Y, Song B, et al. 2006. Specific recognition and accelerated uncoating of retroviral capsids by the TRIM5α restriction factor. *PNAS* 103:5514–19
89. Skrisovska L, Schubert M, Allain FHT. 2009. Recent advances in segmental isotope labeling of proteins: NMR applications to large proteins and glycoproteins. *J. Biomol. NMR* 46:51–65
90. Zinke M, Fricke P, Lange S, Zinn-Justin S, Lange A. 2018. Protein–protein interfaces probed by methyl labeling and proton-detected solid-state NMR spectroscopy. *ChemPhysChem* 19:2457–60
91. Zinke M, Fricke P, Samson C, Hwang S, Wall JS, et al. 2017. Bacteriophage tail-tube assembly studied by proton-detected 4D solid-state NMR. *Angew. Chem. Int. Ed.* 56:9497–501
92. Tissot AC, Renhofa R, Schmitz N, Cielens I, Meijerink E, et al. 2010. Versatile virus-like particle carrier for epitope based vaccines. *PLOS ONE* 5:e9809
93. Hu X, Deng Y, Chen X, Zhou Y, Zhang H, et al. 2017. Immune response of a novel ATR-AP205-001 conjugate anti-hypertensive vaccine. *Sci. Rep.* 7:12580
94. Janitzek CM, Peabody J, Thrane S, Carlsen PHR, Theander TG, et al. 2019. A proof-of-concept study for the design of a VLP-based combinatorial HPV and placental malaria vaccine. *Sci. Rep.* 9:5260
95. Yenkoidiok-Douti L, Williams AE, Canepa GE, Molina-Cruz A, Barillas-Mury C. 2019. Engineering a virus-like particle as an antigenic platform for a Pfs47-targeted malaria transmission-blocking vaccine. *Sci. Rep.* 9:16833
96. Palladini A, Thrane S, Janitzek CM, Pihl J, Clemmensen SB, et al. 2018. Virus-like particle display of HER2 induces potent anti-cancer responses. *OncoImmunology* 7:e1408749
97. Maurer P, Bachmann MF. 2007. Vaccination against nicotine: an emerging therapy for tobacco dependence. *Expert Opin. Investig. Drugs* 16:1775–83
98. Mohsen MO, Augusto G, Bachmann MF. 2020. The 3Ds in virus-like particle based-vaccines: "design, delivery and dynamics." *Immunol. Rev.* 296:155–68
99. Sergeyev IV, Itin B, Rogawski R, Day LA, McDermott AE. 2017. Efficient assignment and NMR analysis of an intact virus using sequential side-chain correlations and DNP sensitization. *PNAS* 114:5171–76
100. Sergeyev IV, Bahri S, Day LA, McDermott AE. 2014. Pf1 bacteriophage hydration by magic angle spinning solid-state NMR. *J. Chem. Phys.* 141:22D533
101. Sergeyev IV, Day LA, Goldbourt A, McDermott AE. 2011. Chemical shifts for the unusual DNA structure in Pf1 bacteriophage from dynamic-nuclear-polarization-enhanced solid-state NMR spectroscopy. *J. Am. Chem. Soc.* 133:20208–17
102. Goldbourt A, Day LA, McDermott AE. 2010. Intersubunit hydrophobic interactions in Pf1 filamentous phage. *J. Biol. Chem.* 285:37051–59
103. Lorieau JL, Day LA, McDermott AE. 2008. Conformational dynamics of an intact virus: order parameters for the coat protein of Pf1 bacteriophage. *PNAS* 105:10366–71

104. Goldbourt A, Day LA, McDermott AE. 2007. Assignment of congested NMR spectra: carbonyl backbone enrichment via the Entner–Doudoroff pathway. *J. Magn. Reson.* 189:157–65
105. Abramov G, Shaharabani R, Morag O, Avinery R, Haimovich A, et al. 2017. Structural effects of single mutations in a filamentous viral capsid across multiple length scales. *Biomacromolecules* 18:2258–66
106. Morag O, Abramov G, Goldbourt A. 2014. Complete chemical shift assignment of the ssDNA in the filamentous bacteriophage fd reports on its conformation and on its interface with the capsid shell. *J. Am. Chem. Soc.* 136:2292–301
107. Morag O, Abramov G, Goldbourt A. 2011. Similarities and differences within members of the Ff family of filamentous bacteriophage viruses. *J. Phys. Chem. B* 115:15370–79
108. Porat G, Lusky OS, Dayan N, Goldbourt A. 2021. Nonuniformly sampled exclusively-$^{13}C/^{15}N$ 4D solid-state NMR experiments: assignment and characterization of IKe phage capsid. *Magn. Reson. Chem.* 59:237–46
109. Liu D, Day L. 1994. Pf1 virus structure: helical coat protein and DNA with paraxial phosphates. *Science* 265:671–74
110. Tsuboi M, Tsunoda M, Overman SA, Benevides JM, Thomas GJ. 2010. A structural model for the single-stranded DNA genome of filamentous bacteriophage Pf1. *Biochemistry* 49:1737–43
111. Welsh LC, Symmons MF, Marvin DA. 2000. The molecular structure and structural transition of the α-helical capsid in filamentous bacteriophage Pf1. *Acta Crystallogr. D* 56:137–50
112. Baltimore D. 1971. Expression of animal virus genomes. *Bacteriol. Rev.* 35:235–41